

Polar Shear Lag Analysis of a Composite of Concentric Cylinders with Longitudinal Cracks: Application to Internal Checking in Wood

J.A.Nairn

Wood Science and Engineering, Oregon State University, Corvallis, OR 97330, USA

Abstract

One potential failure mode for a composite of concentric cylinders is to form microcracks that span the thickness and length of a single cylinder but are arrested at the boundary to the adjacent cylinder (a crack in the r - z plane). This failure mode was analyzed by developing a new polar shear-lag analysis for stresses in a cross section of a concentric cylinders structure. The analysis can accurately calculate hoop and shear stress in each cylinder in the vicinity of microcracks. The stresses were used to calculate the energy release rate for formation of a new microcrack as a tool for predicting the microcracking process due to any source of applied or residual stresses. The target problem was to model internal checking in certain species of trees such as *radiata pine*. In a tree, the alternating regions of early- and latewood that form the growth rings are the concentric cylinders. Internal checking is microcracking in the earlywood layers. The shear-lag analysis was used to predict the propensity of growth rings to form internal checks.

Key words: Shear Lag, Internal Checking, Radiata Pine, Energy Release Rate, Finite Fracture Mechanics

1. Introduction

A common failure mode in layered structures is to develop cracks that span a single layer but stop at the boundary to the adjacent layer. For example, laminates often fail with microcracks in the off-axis plies [1, 2]. Similarly, painted or coated structures, including archival artwork [3], can fail by periodic cracking in the coating layers [4, 5, 6]. Many natural structures are layered as well. For example, the cross-section of a tree is characterized by growth rings of early- and latewood [7]. The alternating early- and latewood regimes create a layered structure of approximately concentric cylinders. Some species, such as *radiata pine*, can fail by internal checking [8, 9, 10], which is cracking of the earlywood layers, most prominently in the sapwood regions adjacent to the heartwood (see Fig. 1). This cracking occurs sometime between harvesting of the tree and final drying. Since the existence of internal checks lowers the value of the wood when it is milled into lumber (due to detrimental effects on appearance), there is a need for analysis methods to model internal checking in layered concentric cylinders. Such an analysis could be a tool for understanding internal checking and for eventually eliminating or ameliorating its effects. It would also have applications for analysis of longitudinal cracking in layers in composite tubes. Predictions of internal checking are consistent with observations and some recommended new experiments are discussed.

Analyses for cracking in laminated composites or in coating/substrate systems have been based on variational mechanics [11] or shear-lag analysis [12, 13, 14] of the structures followed by prediction of cracking based on energy released during the cracking process [15, 1, 2]. Variational mechanics methods are more accurate, but are cumbersome to extend to many layers as would be required for analysis of all growth rings in a tree [16]. Shear lag analysis is a good alternative. Although many shear-lag methods are inaccurate [1], when done correctly, by methods termed optimal or generalized shear lag analysis [12, 13, 14], its accuracy for cracking problems can approach that of variational methods [12, 13]. Prior shear-lag analyses of layered structures considered planar x - y problems that develop cracks in the x - z plane (normal to the y axis) [17, 13, 14] or considered axisymmetric r - z problems that develops cracks in the r - θ plane (normal to the z axis) [17, 12, 14]. The analysis of internal checking, however, requires a new shear-lag analysis

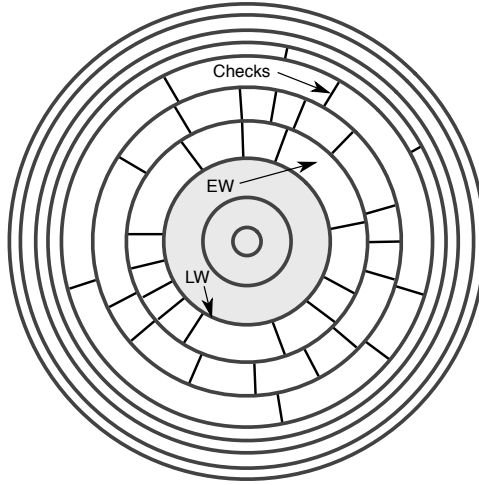


Figure 1: Schematic view of internal checks forming in the earlywood (EW) layers of the cross-section of a tree. The darker rings are thinner latewood (LW) layers. The internal checks usually occur in the sapwood region adjacent to the heartwood region, which is shown in gray.

that considers polar r - θ problems that develop cracks in the r - z plane (normal to the θ , or hoop, direction). This paper develops that new analysis by extending prior optimal shear lag methods to polar analysis of a cross-section of any number of concentric orthotropic cylinders. The analysis accounts for internal and external pressure, for axial load, for thermal- or moisture-induced residual stresses, for any other source of internal stresses, and for imperfect interfaces between the layers. The resulting analysis gives the hoop and shear stresses in each layer for any pattern of cracking on the ends of any wedge of the full cross section. The results were verified by comparison of several sample calculations to finite element analysis calculations and found to be accurate.

To predict layer cracking, the new shear-lag analysis was used to calculate the total energy released as a new crack forms in any one of the cylindrical layers in the structure. The result is expressed in terms of unit energy release rate or energy release per unit stress in that layer. This energy release rate was verified by comparison to finite element analysis. The unit energy release rate can predict the tendency of a layer to form cracks by any mechanism by determining stresses in that layer resulting from that mechanism. Several possible mechanisms were considered. The results suggested an explanation to the formation of internal checks predominantly in rings closer to the center of the tree. Once the cause of internal checking is known, this analysis could make predictions. More experiments are needed, however, to determine the cause or causes of internal checking and to determine key material properties (*i.e.*, toughness) for the checking process. Some potential experiments are discussed.

2. Polar Shear Lag Theory

Figure 2 shows a collection of n concentric cylinders. Cylinder i extends from r_{i-1} to r_i . The figure pictures a solid structure; hollow structures are modeled by having $r_0 > 0$. Each cylinder is assumed to be polar orthotropic with its material r , θ , and z direction properties lined up with the corresponding directions in the structure. Prior shear-lag analysis of such structures have always been for stresses in the r - z plane [14, 12]. This new analysis is for stress in the r - θ plane. In cylindrical coordinates, the shear strain in the r - θ plane is

$$\gamma_{r\theta} = r \frac{\partial(v/r)}{\partial r} + \frac{1}{r} \frac{\partial u}{\partial \theta} \quad (1)$$

where u and v are the r and θ direction displacements. The fundamental shear-lag assumption is to simplify the shear strain by only considering displacements in the direction parallel to the interfaces [14, 13, 12],

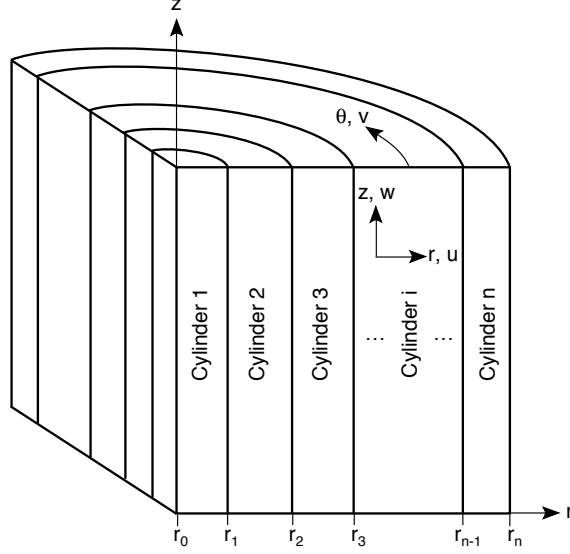


Figure 2: Cylindrical coordinates for a structure of n concentric cylinders. This shear lag analysis is for stresses in the r - θ plane. For wood, r is the radial direction, θ is the tangential direction, and z is the axial or longitudinal direction.

which for polar coordinates is the hoop displacement v . The shear-lag assumption becomes

$$\frac{1}{r} \frac{\partial u}{\partial \theta} \ll r \frac{\partial(v/r)}{\partial r} \quad \text{or} \quad \gamma_{r\theta} \approx r \frac{\partial(v/r)}{\partial r} \quad (2)$$

The r - θ plane shear stress can be written using shape functions that need not be specified until later [14, 13]:

$$\tau_{r\theta}(r, \theta) = \tau(r_{i-1})L_i(r) + \tau(r_i)R_i(r) \quad (3)$$

where $\tau(r_i)$ is the interfacial shear stress at r_i and is a function of θ . $L_i(r)$ is a left-side shape function in cylinder i that varies from $L_i(r_{i-1}) = 1$ to $L_i(r_i) = 0$. $R_i(r)$ is a right-side shape function in cylinder i that varies from $R_i(r_{i-1}) = 0$ to $R_i(r_i) = 1$.

The next step is to multiply the shear stress-strain relation in cylinder i ($\gamma_{r\theta} = G_{r\theta}^{(i)}/\tau_{r\theta}$) by $r((A/r^2) - 1)$ and integrate the radial direction in cylinder i :

$$\int_{r_{i-1}}^{r_i} \left(\frac{A}{r^2} - 1 \right) r \frac{\partial(v/r)}{\partial r} r dr = \int_{r_{i-1}}^{r_i} \left(\frac{A}{r^2} - 1 \right) \frac{\tau_{r\theta}(r, \theta)}{G_{r\theta}^{(i)}} r dr \quad (4)$$

This step adapts a transform technique originally developed by McCartney [17]. It modifies the method for polar coordinates by changing the scaling factor. Repeating the steps of prior analyses [14, 13, 12], this modified method leads to:

$$\begin{aligned} \left\langle \frac{v^{(i+1)}}{r} \right\rangle - \left\langle \frac{v^{(i)}}{r} \right\rangle &= \left\langle \left(\frac{r_{i+1}^2}{r^2} - 1 \right) R_{i+1}(r) \right\rangle \frac{\tau(r_{i+1})}{2G_{r\theta}^{(i+1)}} \\ &+ \left[\frac{1}{2G_{r\theta}^{(i+1)}} \left\langle \left(\frac{r_{i+1}^2}{r^2} - 1 \right) L_{i+1}(r) \right\rangle + \frac{1}{2G_{r\theta}^{(i)}} \left\langle \left(1 - \frac{r_{i-1}^2}{r^2} \right) R_i(r) \right\rangle \right] \tau(r_i) \\ &+ \left\langle \left(1 - \frac{r_{i-1}^2}{r^2} \right) L_i(r) \right\rangle \frac{\tau(r_{i-1})}{2G_{r\theta}^{(i)}} + \frac{v^{(i+1)}(r_i) - v^{(i)}(r_i)}{r_i} \end{aligned} \quad (5)$$

where $\langle \dots \rangle$ indicates the average of any function across the thickness of a layer at fixed angle θ :

$$\left\langle f^{(i)}(r, \theta) \right\rangle = \frac{2}{r_i^2 - r_{i-1}^2} \int_{r_{i-1}}^{r_i} f^{(i)}(r, \theta) r dr \quad (6)$$

The last term in Eq. (5) is the hoop displacement discontinuity at the r_i interface. If the interfaces are assumed to be perfect, this term would be zero, but it is also possible to include imperfect interfaces in a shear lag analysis [14]. Following Hashin [18], the last term is assumed to be proportional to the interfacial shear traction or

$$\frac{v^{(i+1)}(r_i) - v^{(i)}(r_i)}{r_i} = \frac{\tau(r_i)}{r_i D_s^{(i)}} \quad (7)$$

where $D_s^{(i)}$ is an imperfect interface parameter for the r_i interface. $D_s^{(i)} \rightarrow \infty$ models zero discontinuity or a perfect interface; $D_s^{(i)} \rightarrow 0$ models zero stress or a debonded interfaces; any other value models an imperfect interface. Imperfect interfaces are included for completeness, but they are not used in any calculations (there is unlikely to be slip between growth rings in a tree)

For polar-orthotropic materials, the hoop-direction radial strain is related to stresses by:

$$\varepsilon_{\theta\theta} = \frac{u}{r} + \frac{1}{r} \frac{\partial v}{\partial \theta} = \frac{\sigma_{\theta\theta}}{E_\theta} - \frac{\nu_{r\theta} \sigma_{rr}}{E_r} - \frac{\nu_{z\theta} \sigma_{zz}}{E_z} + \alpha_\theta \Delta T + \beta_\theta c_{sat} \Delta \mu \quad (8)$$

where E_r , E_θ , and E_z are the moduli in the three directions, $\nu_{r\theta}$ and $\nu_{z\theta}$ are Poisson ratios, and α_θ and β_θ are the hoop direction thermal and moisture expansion coefficients. ΔT is the temperature difference and $\Delta \mu = c/c_{sat}$ is the concentration potential change. The potential is the moisture content as a fraction of the saturation moisture content. Differentiating with respect to θ , using the shear lag approximation (that $\frac{1}{r} \frac{\partial u}{\partial \theta} \approx 0$), and assuming the θ variations in σ_{rr} and σ_{zz} are much smaller than θ variations in $\sigma_{\theta\theta}$ leads to

$$\frac{\partial^2}{\partial \theta^2} \left(\frac{v}{r} \right) = \frac{1}{E_\theta} \frac{\partial \sigma_{\theta\theta}}{\partial \theta} \quad (9)$$

Unlike some shear-lag descriptions that require transverse stresses (here σ_{rr} and σ_{zz}) to be much smaller than the analysis-direction stresses (here $\sigma_{\theta\theta}$), this approach is more general. This analysis only requires the θ variations in the transverse stresses to be negligible. After all, a planned use of this analysis is for an internally pressurized, layered cylinder where $\sigma_{\theta\theta}$ and σ_{rr} will be of similar magnitude. An analysis that requires the magnitude of σ_{rr} to be negligible would not be accurate.

By cylindrical stress equilibrium

$$\frac{\partial \sigma_{\theta\theta}}{\partial \theta} = -r \frac{\partial \tau_{r\theta}}{\partial r} - 2\tau_{r\theta} \quad (10)$$

Averaging Eqs. (9) and (10) over the layer thickness leads to

$$\frac{\partial^2}{\partial \theta^2} \left\langle \frac{v}{r} \right\rangle = \frac{1}{E_\theta} \frac{\partial \langle \sigma_{\theta\theta} \rangle}{\partial \theta} = \frac{2}{E_\theta^{(i)} (r_i^2 - r_{i-1}^2)} (r_{i-1}^2 \tau(r_{i-1}) - r_i^2 \tau(r_i)) \quad (11)$$

Finally differentiating Eq. (5) twice with respect to θ and using Eq. (11) gives:

$$\begin{aligned} & \frac{-2r_{i+1}^2 \tau(r_{i+1})}{E_\theta^{(i+1)} (r_{i+1}^2 - r_i^2)} + 2r_i^2 \tau(r_i) \left(\frac{1}{E_\theta^{(i+1)} (r_{i+1}^2 - r_i^2)} + \frac{1}{E_\theta^{(i)} (r_i^2 - r_{i-1}^2)} \right) - \frac{2r_{i-1}^2 \tau(r_{i-1})}{E_\theta^{(i)} (r_i^2 - r_{i-1}^2)} = \\ & \left\langle \left(\frac{r_{i+1}^2}{r^2} - 1 \right) R_{i+1}(r) \right\rangle \frac{\tau''(r_{i+1})}{2G_{r\theta}^{(i+1)}} + \left\langle \left(1 - \frac{r_{i-1}^2}{r^2} \right) L_i(r) \right\rangle \frac{\tau''(r_{i-1})}{2G_{r\theta}^{(i)}} + \frac{\tau''(r_i)}{r_i D_s^{(i)}} \\ & + \left[\frac{1}{2G_{r\theta}^{(i+1)}} \left\langle \left(\frac{r_{i+1}^2}{r^2} - 1 \right) L_{i+1}(r) \right\rangle + \frac{1}{2G_{r\theta}^{(i)}} \left\langle \left(1 - \frac{r_{i-1}^2}{r^2} \right) R_i(r) \right\rangle \right] \tau''(r_i) \end{aligned} \quad (12)$$

Equation (12) for $i = 1$ to $n-1$ is a system of $n-1$ second-order differential equations for the $n-1$ interfacial shear stresses. It can be rewritten in matrix form as

$$[A] \frac{d^2 \vec{\tau}_r}{d\theta^2} - [B] \vec{\tau}_r = -\vec{\tau}_{r0} \quad (13)$$

where

$$\vec{\tau}_r = (r_1^2 \tau(r_1), r_2^2 \tau(r_2), \dots, r_{n-1}^2 \tau(r_{n-1})) \quad (14)$$

$$\vec{\tau}_{r0} = \left(\frac{2r_0^2 \tau(r_0)}{E_\theta^{(1)}(r_1^2 - r_0^2)}, 0, \dots, 0, \frac{2r_n^2 \tau(r_n)}{E_\theta^{(n)}(r_n^2 - r_{n-1}^2)} \right) \quad (15)$$

$$(16)$$

where $\tau(r_0) = \tau(r_n) = \tau_0$ is a globally applied in-plane shear stress. For static equilibrium, these applied shear stresses must be equal. This analysis does not include torsion as that would require $\tau_{\theta z}$ and results that depend on z . The elements of the tridiagonal matrices $[A]$ and $[B]$ are

$$A_{i,i-1} = \frac{1}{2r_{i-1}^2 G_{r\theta}^{(i)}} \left\langle \left(1 - \frac{r_{i-1}^2}{r^2} \right) L_i(r) \right\rangle \quad (17)$$

$$A_{i,i} = \frac{1}{r_i^2} \left[\frac{1}{2G_{r\theta}^{(i+1)}} \left\langle \left(\frac{r_{i+1}^2}{r^2} - 1 \right) L_{i+1}(r) \right\rangle + \frac{1}{2G_{r\theta}^{(i)}} \left\langle \left(1 - \frac{r_{i-1}^2}{r^2} \right) R_i(r) \right\rangle + \frac{1}{r_i D_s^{(i)}} \right] \quad (18)$$

$$A_{i,i+1} = \frac{1}{2r_{i+1}^2 G_{r\theta}^{(i+1)}} \left\langle \left(\frac{r_{i+1}^2}{r^2} - 1 \right) R_{i+1}(r) \right\rangle \quad (19)$$

$$B_{i,i-1} = -\frac{2}{E_\theta^{(i)}(r_i^2 - r_{i-1}^2)} \quad (20)$$

$$B_{i,i} = \frac{2}{E_\theta^{(i+1)}(r_{i+1}^2 - r_i^2)} + \frac{2}{E_\theta^{(i)}(r_i^2 - r_{i-1}^2)} \quad (21)$$

$$B_{i,i+1} = -\frac{2}{E_\theta^{(i+1)}(r_{i+1}^2 - r_i^2)} \quad (22)$$

For problems involving cracking, it is useful to have an equation for hoop stresses instead. First rearrange Eq. (13) to:

$$\frac{d^2 \vec{\tau}_r}{d\theta^2} - [M_\tau] \vec{\tau}_r = -[M_\tau] \vec{\tau}_\infty \quad (23)$$

where

$$[M_\tau] = [A]^{-1}[B] \quad \text{and} \quad \vec{\tau}_\infty = [B]^{-1} \vec{\tau}_{r0} \quad (24)$$

Following methods from 0, the i^{th} component of $\vec{\tau}_\infty$ can be derived as

$$(\vec{\tau}_\infty)_i = \tau_0 \left[r_0^2 + (r_n^2 - r_0^2) \frac{\sum_{j=1}^i (r_j^2 - r_{j-1}^2) E_\theta^{(j)}}{\sum_{j=1}^n (r_j^2 - r_{j-1}^2) E_\theta^{(j)}} \right] \quad (25)$$

It can be proved by induction using Eq. (11) that

$$\vec{\tau}_r = r_0^2 \tau_0 (1, 1, \dots, 1) - [I_L] \frac{d\vec{p}}{d\theta} \quad (26)$$

where

$$(\vec{p})_i = \frac{r_i^2 - r_{i-1}^2}{2} \left\langle \sigma_{\theta\theta}^{(i)} \right\rangle \quad (27)$$

and $[I_L]$ is an $(n-1) \times (n-1)$ matrix with all diagonal and lower half-diagonal elements equal to one while all upper half-diagonal elements are zero (*i.e.*, $[I_L]_{i,j} = 1$ if $i \geq j$, otherwise $[I_L]_{i,j} = 0$). Substitution into Eq. (23) gives

$$\frac{d^3 \vec{p}}{d\theta^3} - [M_\sigma] \frac{d\vec{p}}{d\theta} = -[M_\sigma] \frac{d\vec{p}_\infty}{d\theta} \quad (28)$$

where

$$[M_\sigma] = [I_L]^{-1}[M_\tau][I_L] \quad \text{and} \quad \frac{d\vec{p}_\infty}{d\theta} = [I_L]^{-1} (r_0^2 \tau_0(1, 1, \dots, 1) - \vec{\tau}_\infty) \quad (29)$$

Noting that $[I_L]^{-1}$ is 1 if $i = j$, -1 if $j = i - 1$, and 0 otherwise [13], leads to

$$[M_\sigma]_{i,j} = \sum_{k=j}^{n-1} \left([M_\tau]_{i,k} - [M_\tau]_{i-1,k} \right) = \sum_{k=j}^{n-1} \sum_{\ell=k-1}^{k+1} \left([A]_{i,\ell}^{-1} - [A]_{i-1,\ell}^{-1} \right) B_{\ell,k} \quad (30)$$

$$\left(\frac{d\vec{p}_\infty}{d\theta} \right)_i = \tau_0 (r_n^2 - r_0^2) \frac{(r_i^2 - r_{i-1}^2) E_\theta^{(j)}}{\sum_{j=1}^n (r_j^2 - r_{j-1}^2) E_\theta^{(j)}} \quad (31)$$

where $[M_\tau]_{0,k}$, $[A]_{i,0}^{-1}$, $[A]_{0,n}^{-1}$, $B_{0,k}$, and $B_{n,k}$ are taken as zero. Finally, integrating with respect to θ once gives

$$\frac{d^2 \vec{p}}{d\theta^2} - [M_\sigma] \vec{p} = -[M_\sigma] \vec{p}_\infty \quad (32)$$

where \vec{p}_∞ are the far-field hoop stresses in concentric cylinders with no cracks. This equation is a general shear-lag analysis for r - θ plane stress in concentric, polar orthotropic materials. The shear lag ‘‘parameter’’ is the matrix of constants $[M_\sigma]$. This matrix depends on the geometry and mechanical properties of all layers and on their assumed shape functions. The analysis includes any source for applied, internal, or residual stresses by their effect on the far-field stresses in \vec{p}_∞ .

For cracking problems, it is preferable to partition the problem into far field stresses and perturbation stresses. The perturbation stresses, \vec{p}' , are the solution to the problem with boundary conditions that are a difference between the uncracked state (*i.e.*, far-field stresses) and the cracked state. Writing $\vec{p} = \vec{p}' + \vec{p}_\infty$, the equation for perturbation stresses is

$$\frac{d^2 \vec{p}'}{d\theta^2} - [M_\sigma] \vec{p}' = 0 \quad (33)$$

This equation can be solved by an eigenanalysis [13], leading to perturbation tensile stresses:

$$\langle \sigma_{\theta\theta}^{(i)} \rangle = 2 \sum_{j=1}^{n-1} (a_j e^{\lambda_j \theta} + b_j e^{-\lambda_j \theta}) \frac{\psi_{j,i}}{r_i^2 - r_{i-1}^2} \quad (34)$$

where λ_j^2 for $j = 1$ to $n - 1$ are the eigenvalues of $[M_\sigma]$ and $\psi_{j,i}$ is the i^{th} element of the corresponding eigenvector. Because $\tau(r_0)$ and $\tau(r_n)$ are in the far-field stress (*i.e.*, see Eq. (25)), the perturbation shear stresses are defined by

$$\frac{d^2 \vec{\tau}'_r}{d\theta^2} - [M_\tau] \vec{\tau}'_r = 0 \quad \text{or} \quad \vec{\tau}'_r = -[I_L] \frac{d\vec{p}'}{d\theta} \quad (35)$$

Noting that the eigenvalues of $[M_\sigma]$ and $[M_\tau]$ are the same (due to relation in Eq. (29)), the differential equation for $\vec{\tau}'_r$ can be solved to give perturbation interfacial shear stresses

$$\tau(r_i) = \sum_{j=1}^{n-1} (a_j e^{\lambda_j \theta} - b_j e^{-\lambda_j \theta}) \frac{\omega_{j,i}}{r_i^2} \quad (36)$$

where $\omega_{j,i}$ is the i^{th} element of the eigenvector of $[M_\tau]$ for eigenvalue λ_j . Alternatively, the relation between $\vec{\tau}'_r$ and $d\vec{p}'/d\theta$ can be used to derive:

$$\tau(r_i) = - \sum_{k=1}^i \sum_{j=1}^{n-1} (a_j e^{\lambda_j \theta} - b_j e^{-\lambda_j \theta}) \frac{\lambda_j \psi_{j,k}}{r_i^2} \quad (37)$$

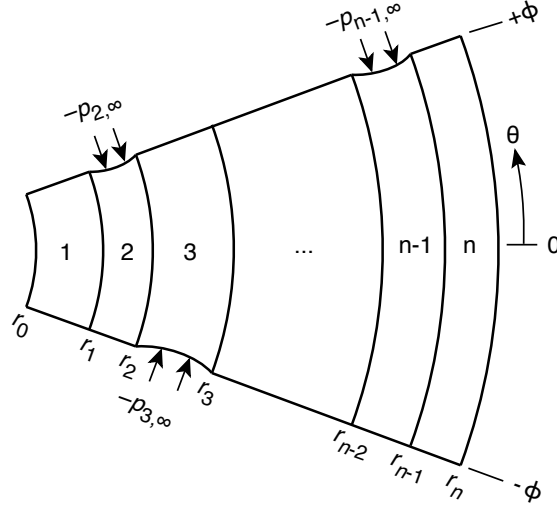


Figure 3: The shear lag analysis always focuses on a wedge of some angle cut from the r - θ plane of the structure. The wedge is selected such that all cracks are one of the two boundaries.

These two solutions are identical because it can be shown that the eigenvectors of $[M_\sigma]$ and $[M_\tau]$ are related by

$$\omega_{j,i} = - \sum_{k=1}^i \lambda_j \psi_{j,k} \quad \text{or} \quad \psi_{j,i} = \frac{\omega_{j,i-1} - \omega_{j,i}}{\lambda_j} \quad (\text{using } \omega_{j,0} = 0) \quad (38)$$

For example, Fig. 3 shows a radial slice of concentric cylinders extending from $-\phi$ to ϕ with some layers cracked on either end while the remaining layers are intact. All cracks are on the boundaries and at least one layer is intact on each boundary. The boundary conditions for the perturbation stresses are

$$\begin{cases} p'_i(\pm\phi) = -p_{\infty,i} & \text{if layer } i \text{ cracked at } \pm\phi \\ \left\langle \frac{v'^{(i)}(\pm\phi)}{r} \right\rangle = 0 & \text{if layer } i \text{ intact at } \pm\phi \end{cases} \quad (39)$$

This problem is solved by finding the unknown constants a_j and b_j . The process for arbitrary boundary conditions is outlined in the appendix.

3. Finite Fracture Mechanics of Layer Cracking

A common failure mode in layered structures is to develop periodic microcracks within one or more layers [19, 1, 2]. In this failure mode, instantaneous cracks appear that span a single layer. If the neighboring layers are tougher (or release insufficient energy when cracked), the crack may arrest at the boundary to that layer. On continued loading the cracking layer develops more cracks as a series of failure events. In cracking of coatings and plies in composites, the preferred approach for modeling and predicting such cracks is to use finite fracture mechanics [15, 20, 21]. In finite fracture mechanics, one calculates the energy released per unit fracture area (ΔG or finite energy release rate) when the next crack spanning a single layer forms. That crack is predicted to occur when the total energy released exceeds a characteristic material property of toughness for the considered layer-cracking phenomenon. This section uses the new shear lag analysis to calculate finite energy release rate associated with layer cracking in cylindrical structures.

Figure 4 shows the formation of a new crack between two existing cracks in a single layer where all cracking is confined to a single layer (the generalization to cracking of any layer in a slice with any prior

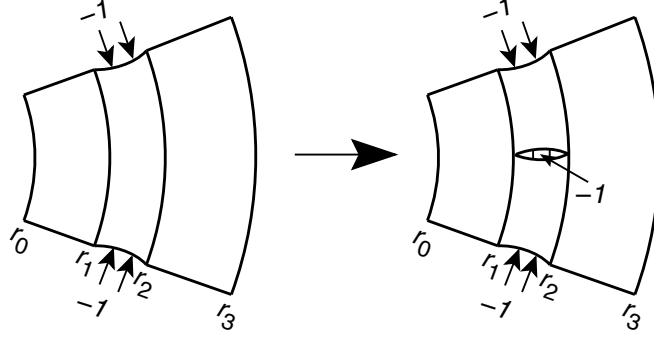


Figure 4: The formation of a new crack in layer 2 between two existing cracks in a three-layer structure. For the perturbation stress analysis and unit energy release rate, the stress on the crack surfaces is set to -1.

existing cracks is straightforward). The boundary conditions show only the perturbation stresses because by composite fracture mechanics [22], the finite energy release rate is given by:

$$\Delta G = \frac{\Delta U_p(\phi)}{\Delta A} = \frac{\Delta \left(\frac{1}{2} \int_S \vec{T}^p \cdot \vec{u}^p dS \right)}{\Delta A} \quad (40)$$

where U_p is the perturbation strain energy and ΔA is the new crack surface area. U_p can be found from a surface integral over the perturbation tractions (\vec{T}^p) and displacements (\vec{u}^p). On the top surface, $T^p \cdot \vec{u}^p = -\sigma_\infty^{(i)} v'^{(i)}(\phi)$; on the bottom surface, $T^p \cdot \vec{u}^p = \sigma_\infty^{(i)} v'^{(i)}(-\phi)$; here $\sigma_\infty^{(i)} = 2p_{\infty,i}/(r_i^2 - r_{i-1}^2)$ is the far-field hoop stress in layer i . The perturbation energy becomes:

$$U_p(\phi) = \frac{\ell}{2} \left[\sum_{i(\text{bottom cracks})} p_{\infty,i} \left\langle \frac{v'^{(i)}(-\phi)}{r} \right\rangle - \sum_{i(\text{top cracks})} p_{\infty,i} \left\langle \frac{v'^{(i)}(\phi)}{r} \right\rangle \right] \quad (41)$$

where the sums are over the crack layers on the bottom or top surface and ℓ is the z -direction length. When a single layer is cracked on both the top and bottom surface (see Fig. 4), the perturbation energy simplifies to

$$U_p(\phi) = -\ell \left(\frac{r_i^2 - r_{i-1}^2}{2} \right) (\sigma_\infty^{(i)})^2 \left\langle \frac{\hat{v}^{(i)}(\phi)}{r} \right\rangle \quad (42)$$

where $\hat{v}^{(i)}(\phi)$ is the hoop displacement due unit perturbation stress at $\pm\phi$ (by linearity, $v'^{(i)}(\phi) = \sigma_\infty^{(i)} \hat{v}^{(i)}(\phi)$).

Finally, the energy release rate due to formation of a new crack midway between the existing cracks (see Fig. 4) is

$$\Delta G(\rho) = \frac{2U_p(\phi/2) - U_p(\phi)}{\ell(r_i - r_{i-1})} = -\bar{r}_i (\sigma_\infty^{(i)})^2 \left(2 \left\langle \frac{\hat{v}^{(i)}(\phi/2)}{r} \right\rangle - \left\langle \frac{\hat{v}^{(i)}(\phi)}{r} \right\rangle \right) \quad (43)$$

where $\bar{r}_i = (r_i + r_{i-1})/2$ is the midpoint of layer i and $\rho = 1/(2\phi\bar{r}_i)$ is the crack density (cracks per mm) in the layer. To find the energy release rate for cracking of one layer under a variety of loading condition, the first step is to solve the perturbation stress problem with unit normal compression on the crack surfaces at $\pm\phi$. From the average displacement on the ends on the cracked layers, a unit energy release rate is defined by

$$\Delta G_{unit}(\rho) = -\bar{r}_i \left(2 \left\langle \frac{\hat{v}^{(i)}(\phi/2)}{r} \right\rangle - \left\langle \frac{\hat{v}^{(i)}(\phi)}{r} \right\rangle \right) \quad (44)$$

The energy release rate for a variety of fracture problems is then found from

$$\Delta G = (\sigma_\infty^{(i)})^2 \Delta G_{unit}(\rho) \quad (45)$$

This equations separates the energy release rate analysis from the far-field stresses in the layers. Once the unit stress problem is solved, any potential mechanism for internal checking can be analyzed simply by calculating the far-field stresses caused by that mechanism. Some possible mechanisms are discussed the next section.

4. Example Calculations

The first example calculation was for a 3-layer carbon fiber/epoxy composite hollow tube with $(r_0, r_1, r_2, r_3) = (10.0, 10.5, 11.0, 11.5)$ mm. The inner and outer layers were 90° plies with the fibers wrapping in the hoop direction. The interior layer was a 0° ply with the fibers running in the axial direction. Under internal pressurization, such tubes are susceptible to cracks in the interior ply that span the width of the ply (in the radial direction) and length of the tube (in the axial direction). All plies were assumed to be transversely isotropic with the fibers in the axial direction and properties $E_A = 128.0$ GPa, $E_T = 7.3$ GPa, $G_A = 4.0$ GPa, $\nu_T = 0.5$, and $\nu_A = 0.3$. Assuming plane-strain analysis, the inner and outer plies had

$$E_\theta = \frac{E_A}{1 - \nu_A \nu'_A} = 128.7 \text{ GPa}, \quad G_{r\theta} = G_A = 4.0 \text{ GPa}, \quad \nu'_A = \frac{E_T \nu_A}{E_A} \quad (46)$$

The interior ply had plane-strain properties

$$E_\theta = \frac{E_T}{1 - \nu_A \nu'_A} = 7.34 \text{ GPa}, \quad G_{r\theta} = \frac{E_T}{2(1 - \nu_T)} = 2.43 \text{ GPa} \quad (47)$$

The sample calculation was for a 15° slice with cracks on both ends of the interior ply. The results are in Fig. 5. The grid shows a finite element analysis (FEA) grid used to verify the shear-lag calculations. The analysis was for perturbation stress and thus the interior ply was loaded with unit compression stress on the two crack ends while the inner and outer plies were held at zero displacement. The plot in Fig. 5 shows the hoop stress in the interior play and the interfacial shear stresses along the r_1 and r_2 interfaces. The solid lines are the shear-lag analysis; the dotted lines are the FEA. The FEA grid actually used more elements than show in Fig. 5, but the extra elements were left out for clarity. Furthermore, the FEA used the same anisotropic ply properties, but the axes of each element were rotated to match local fiber orientation. The shear lag and FEA results agreed well. The FEA results for hoop stress is the average stress in the layer found by averaging in the radial direction.

These calculations were repeated for 1.0 mm thick plies rather than 0.5 mm plies or with $(r_0, r_1, r_2, r_3) = (10.0, 11.0, 12.0, 13.0)$ mm. Figure 6 compares two different shear lag calculations (solid lines) to the FEA results (dashed line). First, the shear-lag analysis was divided into three layers corresponding to the three physical layers. This analysis differed from the FEA results. But, there is no reason the shear lag analysis has to be limited to physical layers. To improve accuracy, each physical layer can be subdivided into additional layers. The “5 layers” result is the shear lag stress where the each ply was subdivided into five, 0.2 mm layers; the plotted stress is the average stress over the five layers in the interior ply. This refined analysis and the FEA agreed well.

The motivation for this work was for many concentric cylinders rather than a few. The specific problem was an idealized structure of a tree where the concentric cylinders are the growth rings. Figure 7 shows a wedge from the cross-section of tree with four growth rings, each with a thicker earlywood layer (lighter shade) and a thinner latewood layer (darker shade). The central core (darkest shade) is a heart wood zone. This structure was constructed as follows. First, the heart wood zone and first earlywood zone were set (arbitrarily) to be 8 mm and 10 mm thick, respectively. Next, each growth ring (one earlywood layer and the next latewood layer) was assumed to have constant basal area (*i.e.*, $r_i^2 - r_{i-2}^2$ for $i = 3, 5, 7, 9$, equal to a constant). Finally, 80% of each layer was earlywood with the remaining being latewood. The resulting final outside diameter was 36.93 mm.

The properties of the early- and latewood layers were taken from the numerical study in 0. For the shear-lag analysis here, all that was needed were E'_θ and $G_{r\theta}$ for each layer under plane strain conditions. The properties used were $E'_\theta = E_\theta / (1 - \nu_{\theta z} \nu_{z\theta}) = 164$ MPa and $G_{r\theta} = 50$ MPa for earlywood and $E'_\theta = 1238$ MPa

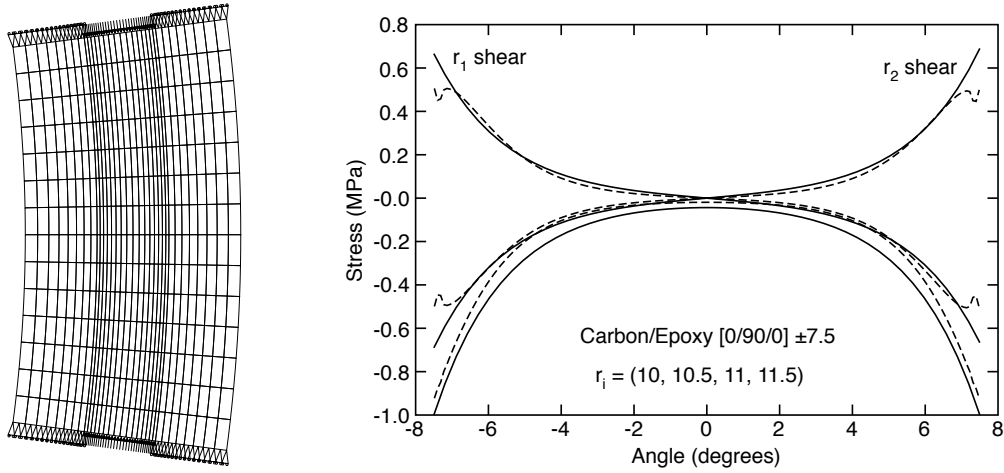


Figure 5: Stresses in the central ply of a three-layer composite tube. The left shows the FEA grid. The right should the stresses by shear lag analysis or by finite element analysis (dotted lines). The three stresses are the hoop stress in the interior ply and the interfacial shear stresses at the r_1 and r_2 interfaces.

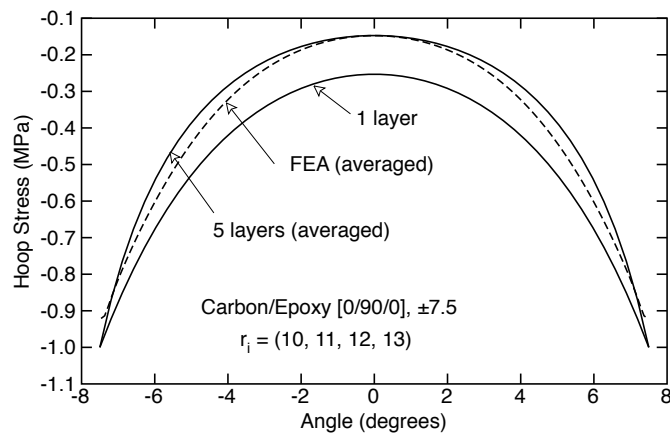


Figure 6: Hoop stress in the interior cracked layer of a three-layer carbon/epoxy composite tube. The solid lines are shear lag analysis and the dotted line is finite element analysis. The “1 layer” shear lag analysis use one analysis layer per physical layer; the “5 layer” shear lag analysis subdivided each physical layer into 5 analysis layers. The plotted result is an average of the 5 layers in the interior ply.

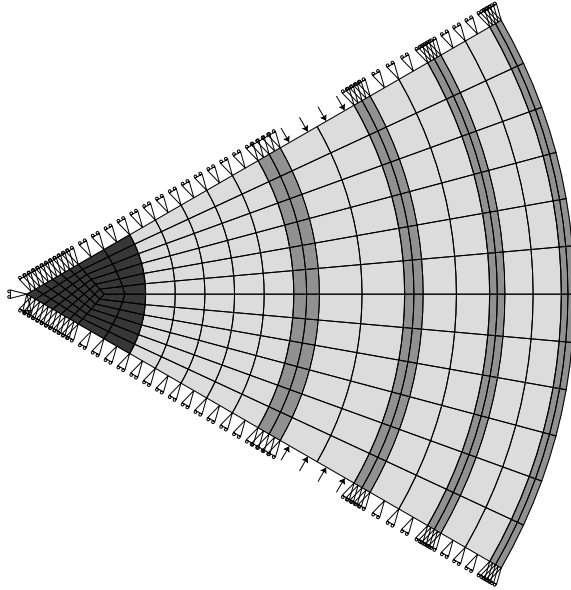


Figure 7: Geometry and finite element grid for analysis of a wedge of a tree with a heartwood zone (darkest region) and four growth rings or earlywood (lightest shade) and latewood (medium shade). The area of the growth rings is constant. The boundary conditions show cracks on both ends of the earlywood region in the second growth ring.

and $G_{r\theta} = 215$ MPa for latewood [23]. The heartwood zone was arbitrarily set to bulk wood orthotropic properties leading to $E'_\theta = 1000$ MPa and $G_{r\theta} = 80$ MPa [23]. For a stress analysis with layer cracks, the second earlywood layer (between r_3 and r_4) was assumed to be cracked. Figure 7 shows the boundary conditions for the perturbation stresses with unit compression stress on the second earlywood layer and zero displacement on the ends of the remaining layers. The solid lines in Fig. 8 show the hoop stress in the cracked earlywood layer and the shear stresses at the inner and outer interfaces from the cracked earlywood layer to the adjacent latewood layer. The dashed lines are FEA results and they agreed well with the shear-lag analysis (the FEA analysis used the full orthotropic properties for early- and latewood in 0). Note that the shear-lag analysis worked well even with only one analysis layer per physical material layer and even with fairly thick layers. We suggest that thick layers work better in wood structures than in the carbon fiber/epoxy tubes due to the smaller differences between the layer moduli. A misconception in the literature is that shear-lag analysis requires at high contrast between layer moduli. This misconception developed because some early shear-lag models were developed specifically for the high modulus contrast limit [24]. When shear lag is developed optimally, it works for any modulus ratio [13, 12].

The final example was to calculate the energy release rate associated with the formation of a new crack within an early or latewood layer and as a function of the position of the layer in the tree. This example considered crack formation in each layer while all other layers were uncracked. Figure 9 shows the unit energy release rate (Eq. (44)) for each early- and latewood layer as a function of the current crack density in the layer. All energy release rates are highest at low crack density and decrease as the number of cracks increases. The pattern is identical to cracking in many other layered structures [1, 2]. Between early- and latewood layers, the unit energy release rate is much higher in the earlywood layers. Considering location of the layer, the energy release rate is highest in the earlywood ring closest to the pith (or center) of the tree and decreases as location gets farther from the pith. The highest energy release rate among latewood rings is also the ring closest to the pith, but does not monotonically decrease when moving away from the pith. The symbols are FEA results for the two inner-most earlywood layers. Each FEA point required two FEA calculations at the current crack density and at twice the crack density. The energy release rate was found by subtracting the total strain energies (Eq. (40)). The FEA results and shear-lag analyses agreed

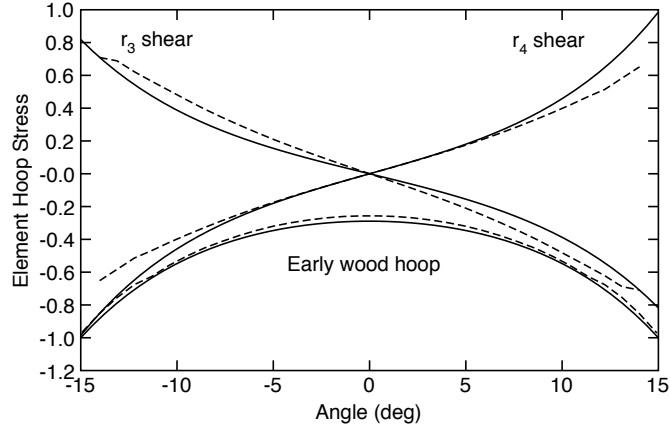


Figure 8: Hoop stress in the cracked earlywood layer and the interfacial shear stress on inner and outer edges of that earlywood layer. The solid lines are by shear lag analysis. The dotted lines are by finite element analysis. The finite element grid is show in Fig. 7.

well. The differences between early- and latewood layers and between different positions in the tree depend on both the properties and the thickness of the layers. The thickness effect is probably significant. Although thickness dependence is not obvious in Eq. (44), the corresponding analysis for cracking in planar layers shows that energy release rate is proportional to thickness. The consequence in planar laminates is that thicker layers are more prone to cracking [1, 2].

Finite Fracture Mechanics for Internal Checking

In finite fracture mechanics of layer cracking, the next crack is assumed to form when ΔG is equal to or greater than $G_c^{(i)}$ or the toughness of layer i for that cracking process. Solving Eq. (45) for layer stress, the crack will form when

$$\sigma_\infty^{(i)} = \sqrt{\frac{G_c^{(i)}}{\Delta G_{unit}(\rho)}} \quad (48)$$

This equation can be used in two ways. First, if $G_c^{(i)}$ is known for all layers and one can calculate $\sigma_\infty^{(i)}$ for any applied loading mechanism, Eq. (48) can predict if that stress could cause internal checking. Second, if one can measure $\sigma_\infty^{(i)}$ at the formation of internal checks, Eq. (48) can be used to determine $G_c^{(i)}$ or the checking toughness of the layer that cracked. Each of these uses is discussed in this section.

Since internal checks form sometime between harvesting a log and cool down after kiln drying, the only sources of stresses are differential thermal expansion as the log is heated in the kiln, differential moisture and thermal shrinkage as the log is dried and cooled down, and water stress caused by hydrostatic tension in the cell lumens at the beginning of drying. Residual stresses by differential thermal or moisture expansions are known to cause layer cracking in composite laminates [1, 25]. The cracking occurs because the 90° ply thermal expansion is much higher than the 0° ply thermal expansion and thus cooling leads to tension in the 90° plies. For the same mechanism to cause cracking in wood, similar differential shrinkage would need to occur. When the log is first heated in the kiln, checking could occur if the tangential thermal expansion of the earlywood layers was much lower than the latewood layers. Similarly, drying and cooling the log could cause checking if the thermal and/or moisture expansion of the earlywood layers was much higher than the latewood layers. Prediction of checking by residual stresses requires thermal and moisture expansion coefficients. Although these are known for bulk wood, there are few results for separate early- and latewood properties. According to 0 the earlywood layers of *radiata pine* experience moisture shrinkage of 1.8–6.9% from fiber saturation to 12% moisture content and the latewood layer in the same ring shrinks about 0.5% more. Thus the moisture expansion properties are similar for early- and latewood with latewood being slightly higher. It is likely the thermal expansion properties are also similar. The bulk thermal expansion

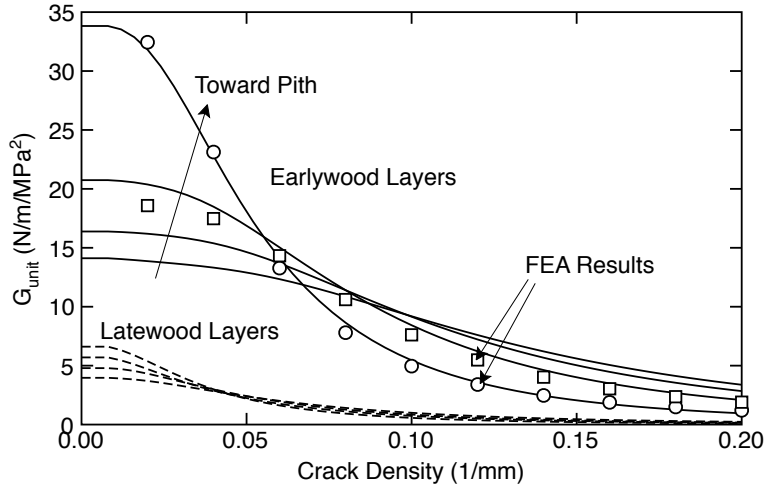


Figure 9: The unit energy release rate (N/m/MPa^2) for cracking of each layer in the structure shown in Fig. 7. The earlywood layers (solid curves) have higher energy release rate and it increases as the layer gets closer to the center. The latewood layers (dashed curves) had lower energy release rate and no monotonic variation with position. The symbols are FEA results for the two earlywood layers closest to the pith.

of porous media is determined by the properties of the solid material and not by the volume pores (*e.g.*, the thermal expansion of styrofoam is the same as the thermal expansion of polystyrene). Thus, even though latewood cells have thicker cell walls and small cell lumens, the thermal expansion of latewood is unlikely to differ significantly from earlywood unless the material properties of the cell walls change significantly as well. These results suggest that differential strains caused by residual stresses are unlikely to cause internal checks. If they do, the most likely cause would be thermal expansion when first heated in the kiln. Although the total stress developed might be small, the earlywood layers are likely to have a lower $G_c^{(i)}$ in the green state and thus by Eq. (48), less residual stress would be needed to cause cracking.

Prior discussions on internal checking have suggested water stress caused by hydrostatic tension in the water that fills the cell lumen may be sufficient to cause the checking [8, 10]. An approximate analysis suggests that this stress will cause tension in the earlywood layers [8]. Due to the thicker cell walls and smaller cell lumens in the latewood, the same mechanism would cause little stress in the latewood zones. In other words, water stress would cause differential strain between early- and latewood that could cause tensile $\sigma_\infty^{(i)}$ in the earlywood layers. Since neither the magnitude of the water stress nor $G_c^{(i)}$ are known, it is not possible to make definitive predications about checking. It is certainly a reasonable mechanism for checking. Furthermore, if the water stress is similar between growth rings, the unit energy release rate provides an explanation for the preference of internal checks to form in layers closer to the center of the tree (see Fig. 9).

A missing material property for better analysis of internal checking is determination of $G_c^{(i)}$. Furthermore, this toughness may change as a function of position in the tree just as other properties change from the inner rings (juvenile wood) to the outer rings (mature wood) [7]; it may also change as a function of temperature and moisture content. The toughness of each layer is a material property and can only be determined by experiments. Two methods for measure checking toughness can be suggested. The most direct route is by direct observation of earlywood checks. In previous work, internal checks have only been observed in the final state [8, 10, 9]. This information is insufficient for determining toughness. The experimental goal should follow the analogous work in composite laminates which tracked the density of microcracks as a function of known applied stress [1]. The goal for checking experiments would be to monitor the density of internal checks as a function of known far-field applied stress in the layers. One potential experiment would be to cut a disk of wood from a tree, remove the heartwood to produce a hollow disk, and load the disk by internal pressure. This loading state would cause a known level of hoop tension that may lead to

internal checks that could be interpreted using Eq. (48). An alternative to direct observation of checks is to propagate radial cracks in the transverse plane [26]. The goal would be to monitor energy release rate during crack propagation and potentially resolve the toughness as a function of position and changes in toughness between early- and latewood zones. Work on these two possible experiments is in progress.

5. Conclusion

A new polar shear-lag analysis was developed to predict stress in the transverse plane of concentric-cylinder composites containing longitudinal cracks in some of the layers. This analysis was very similar to prior shear-lag analysis but extends shear-lag methods to new classes of problems. The analysis was used here to investigate the mechanics of internal checking in the earlywood layers of wood. By finite fracture mechanics methods, the most likely growth rings to experience checking are the earlywood layers closest to the pith. This finding is consistent with experimental observations. A more thorough investigation of internal checking requires new methods for determining internal stress in the wood and new experiments for measuring the toughness of earlywood layers. This toughness is likely to depend on position in the tree, on temperature, and on moisture content.

Acknowledgements

This work was supported by a contract from the Wood Quality Initiative (WQI), New Zealand.

Appendix

The shear-lag solution process for an arbitrary number of concentric cylinders with arbitrary distributions of cracks located at $\pm\phi$ is outlined in this appendix.

1. Find the $[A]$ and $[B]$ matrices. The key step here is to select the shape functions needed for $[A]$. First, the shape function can be transformed using a dimensionless coordinate:

$$z_i = \frac{r_i^2 - r^2}{r_i^2 - r_{i-1}^2} \quad \text{and defining} \quad k_i = \frac{r_i^2}{r_i^2 - r_{i-1}^2} \quad (49)$$

z_i is 1 at r_{i-1} and 0 at r_i . The shape function averages required for $[A]$ transform to

$$\left\langle \left(1 - \frac{r_{i-1}^2}{r^2} \right) L_i(r) \right\rangle = \int_0^1 \frac{1 - z_i}{k_i - z_i} L_i(z_i) dz_i \quad (50)$$

$$\left\langle \left(\frac{r_{i+1}^2}{r^2} - 1 \right) L_{i+1}(r) \right\rangle = \int_0^1 \frac{z_{i+1}}{k_{i+1} - z_{i+1}} L_{i+1}(z_{i+1}) dz_{i+1} \quad (51)$$

$$\left\langle \left(1 - \frac{r_{i-1}^2}{r^2} \right) R_i(r) \right\rangle = \int_0^1 \frac{1 - z_i}{k_i - z_i} R_i(z_i) dz_i \quad (52)$$

$$\left\langle \left(\frac{r_{i+1}^2}{r^2} - 1 \right) R_{i+1}(r) \right\rangle = \int_0^1 \frac{z_{i+1}}{k_{i+1} - z_{i+1}} R_{i+1}(z_{i+1}) dz_{i+1} \quad (53)$$

In principle, any shape function can be used, which means this shear lag analysis can be optimized for a particular problem by selecting optimal shape functions. All calculations in this paper used the simplest linear shape functions or assumed $L_i(z_i) = z_i$ and $R_i(z_i) = 1 - z_i$. For these shape functions, the averages evaluate to

$$\left\langle \left(1 - \frac{r_{i-1}^2}{r^2} \right) L_i(r) \right\rangle = -\frac{1}{2} - k_i + k_i^2 \ln \left(\frac{k_i}{k_i - 1} \right) \quad (54)$$

$$\left\langle \left(\frac{r_{i+1}^2}{r^2} - 1 \right) L_{i+1}(r) \right\rangle = \frac{1}{2} + (k_{i+1} - 1) - (k_{i+1} - 1)k_{i+1} \ln \left(\frac{k_{i+1}}{k_{i+1} - 1} \right) \quad (55)$$

$$\left\langle \left(1 - \frac{r_{i-1}^2}{r^2} \right) R_i(r) \right\rangle = \frac{1}{2} - (k_i - 1) + (k_i - 1)^2 \ln \left(\frac{k_i}{k_i - 1} \right) \quad (56)$$

$$\left\langle \left(\frac{r_{i+1}^2}{r^2} - 1 \right) R_{i+1}(r) \right\rangle = -\frac{1}{2} + k_{i+1} - k_{i+1}(k_{i+1} - 1) \ln \left(\frac{k_{i+1}}{k_{i+1} - 1} \right) \quad (57)$$

If the first cylinder is solid ($r_0 = 0$), the only average needed evaluates in a special case to

$$\left\langle \left(1 - \frac{r_0^2}{r^2} \right) R_1(r) \right\rangle = \langle R_1(r) \rangle = \frac{1}{2} \quad (58)$$

2. Find the eigenvalues of $[M_\tau]$. Although $[M_\tau]$ is a real, positive definite matrix, it is not symmetric. From the definition of $[M_\tau]$, the eigenvalue problem can be expressed as finding the $n - 1$ roots to

$$\det([B] - \lambda^2[A]) = 0 \quad (59)$$

where $[A]$ and $[B]$ are tridiagonal matrices. Furthermore, all roots are known to fall between

$$\sqrt{\chi_{min}} \leq \lambda^2 \leq \sqrt{\chi_{max}} \quad (60)$$

where χ are the eigenvalues of the symmetric matrix $[M_\tau][M_\tau]^T$. Here the eigenvalues of the symmetric matrix were found using a stable algorithm [27]. These results were used as initial guesses for finding the $n - 1$ roots to Eq. (59).

3. The eigenvectors are solutions to $[B]\vec{\omega}_j = \lambda_j^2[A]$. Making use of the tridiagonality of $[A]$ and $[B]$ leads to $\omega_{j,1} = 1$,

$$\omega_{j,2} = \frac{B_{11} - \lambda^2 A_{11}}{\lambda^2 A_{12} - B_{12}} \quad (61)$$

$$\omega_{j,i+1} = \frac{(B_{i,i-1} - \lambda^2 A_{i,i-1})\omega_{j,i-1} + (B_{i,i} - \lambda^2 A_{i,i})\omega_{j,i}}{\lambda_j^2 A_{12} - B_{12}} \quad \text{for } i = 2 \text{ to } n - 1 \quad (62)$$

The eigenvectors $\vec{\psi}_l$ are found using Eq. (38).

4. The previous steps depend only on the geometry and properties of the cylinders and not on the boundary conditions. Those steps thus only need to be done once for each structure. The next step is to turn to a specific problem. As illustrated Fig. 3 the angle θ is chosen to vary from $-\phi$ to ϕ . The slice is also chosen such that all cracks are at $\pm\phi$. If there are interior cracks, reduce the size of the slice to accommodate them. Finally, at least one layer on each end must be intact.
5. On each boundary, locate the first intact layer, layer k , and set $\langle v^{(k)}/r \rangle = 0$. By rewriting Eq. (5)

$$\left\langle \frac{v^{(i+1)}}{r} \right\rangle - \left\langle \frac{v^{(i)}}{r} \right\rangle = A_{i,i-1}\tau_{r,i-1} + A_{i,i}\tau_{r,i} + A_{i,i+1}\tau_{r,i+1}, \quad (63)$$

using $\langle v^{(k)}/r \rangle = 0$ as a reference, and iterating forward and backward from layer k , all displacements on the boundary can be written as

$$\vec{V} = [D][\Omega(\theta)]\vec{a} \quad (64)$$

where $V_i = \langle v^{(i)}/r \rangle$ (for $1 = 1$ to n), $\vec{a} = (a_1, b_1, a_2, b_2, \dots, a_{n-1}, b_{n-1})$,

$$[D] = \left[\begin{array}{cc|cc} & & -A_{k-1,k} & \\ & & \vdots & [0]_{k-1,n-k-1} \\ & -[I_L]_{k-1}^T [A]_{1 \rightarrow k-1} & -A_{k-1,k} & \\ \hline 0 \dots 0 & 0 & 0 & 0 \dots 0 \\ \hline [0]_{n-k,k-2} & A_{k,k-1} & & \\ & \vdots & & \\ & A_{k,k-1} & [I_L]_{n-k} [A]_{k \rightarrow n-1} & \end{array} \right] \quad (65)$$

and

$$[\Omega(\theta)] = \begin{bmatrix} \omega_{1,1}e^{\lambda_1\theta} & -\omega_{1,1}e^{-\lambda_1\theta} & \omega_{2,1}e^{\lambda_2\theta} & \dots & -\omega_{n-1,1}e^{-\lambda_{n-1}\theta} \\ \omega_{1,2}e^{\lambda_1\theta} & -\omega_{1,2}e^{-\lambda_1\theta} & \omega_{2,2}e^{\lambda_2\theta} & \dots & -\omega_{n-1,2}e^{-\lambda_{n-1}\theta} \\ \vdots & \vdots & \vdots & \ddots & \vdots \\ \omega_{1,n-1}e^{\lambda_1\theta} & \dots & \dots & \dots & -\omega_{n-1,n-1}e^{-\lambda_{n-1}\theta} \end{bmatrix} \quad (66)$$

where $[A]_{i \rightarrow j}$ is square portion of $[A]$ including rows and columns i to j , $[I_L]_n$ is a square matrix of size n defined for Eq. (26), and $[0]_{i,j}$ is a matrix of zeros of dimension $i \times j$. Setting $\theta = \pm\phi$, depending on boundary being considered, the matrix $[D][\Omega(\pm\phi)]$ is a $n \times 2(n-1)$ matrix that relates the n end displacements to the $2(n-1)$ unknown constants.

6. Express the perturbation layer stresses as

$$\vec{p}^T = [S]\vec{a} \quad (67)$$

where \vec{p}^T is extended to n to include all layers and

$$[S] = \begin{bmatrix} [\Psi(\theta)] \\ \hline -(1, 1, \dots, 1) \cdot [\Psi(\theta)] \end{bmatrix} \quad (68)$$

and $[\Psi(\theta)]$ is analogous to $[\Omega(\theta)]$ with all $\omega_{j,i}$ replaced by $\psi_{j,i}$ and the minus signs on the even columns omitted. Setting $\theta = \pm\phi$, depending on boundary being considered, the matrix $[S]$ is a $n \times 2(n-1)$ matrix that relates the n end stresses to the $2(n-1)$ unknown constants.

7. Finally, iterate over the n ends at $+\phi$ and the n ends at $-\phi$ and construct a system of equations for the unknown constants

$$[C]\vec{a} = \vec{r} \quad (69)$$

Skip the reference intact layer k . For the remaining $n-1$ layers on each end determine if the layer is intact or cracked. If it is intact, transfer the corresponding row from the $[D][\Omega(\pm\phi)]$ matrix to $[C]$ and set the element of \vec{r} to 0. If it is cracked, transfer the corresponding row from the $[S]$ matrix to $[C]$ and set the element of \vec{r} to $-p_{\infty,i} = -(r_i^2 - r_{i-1}^2) \langle \sigma_{\infty}^{(i)} \rangle / 2$. Solve the resulting $2(n-1)$ equations for \vec{a} .

8. A simple Java application was written to input number of layers, properties and thickness of each layer, the size of the wedge, and whether the ends of each layer are intact or crack [28]. That information and the above steps are sufficient to solve for all constants and thereby determine hoop stress, shear stress, hoop displacement, and energy release rate for all calculations in this paper.

References

- [1] J. A. Nairn, S. Hu, Micromechanics of damage: A case study of matrix microcracking, in: R. Talreja (Ed.), *Damage Mechanics of Composite Materials*, Elsevier, Amsterdam, 1994, pp. 187–243.
- [2] J. A. Nairn, Matrix microcracking in composites, in: R. Talreja, J.-A. E. Manson (Eds.), *Comprehensive Composite Materials*, Vol. 2, Elsevier Science, 2000, pp. 403–432.
- [3] M. F. Mecklenberg, M. H. McCormick-Goodhart, C. S. Tumosa, Investigation into the deterioration of paintings and photographs using computerized modeling of stress development, *J. Amer. Inst. of Conservation* 55 (1994) 153–170.
- [4] Y. Leterrier, L. Boogh, J. Andersons, J.-A. E. Manson, Adhesion of silicon oxide layers on poly(ethylene terephthalate). I: Effect of substrate properties on coating's fragmentation process, *J. Polym. Sci., Part B: Polymer Physics* 35 (1997) 1449–1461.
- [5] S. R. Kim, J. A. Nairn, Fracture mechanics analysis of coating/substrate systems subjected to tension or bending loads ii: Experiments in bending, *Engr. Fract. Mech.* 65 (2000) 595–607.
- [6] S. R. Kim, J. A. Nairn, Fracture mechanics analysis of coating/substrate systems subjected to tension or bending loads i: Theory, *Engr. Fract. Mech.* 65 (2000) 573–593.
- [7] J. G. Haygreen, J. L. Bowyer, *Forest Products and Wood Science: An Introduction*, Iowa State University Press, Ames, Iowa, USA, 1996.
- [8] R. E. Booker, Collapse or internal checking — which comes first?, in: *4th IUFRO Wood Drying Conferences*, Vol. Rotorua, New Zealand, 9-13, August, 1994, pp. 133–140.

- [9] S. Pang, R. Orchard, D. McConchie, Tangential shrinkage of pinus radiata earlywood and latewood, and its implication for within-ring internal checking, *New Zealand Journal of Forestry Science* 29 (3) (1999) 484–491.
- [10] R. E. Booker, T. N. Haslett, J. A. Sole, Acoustic emission study of within-ring internal checking in radiata pine-wood ndt 2000, in: 12th International Symposium on Nondestructive Testing of Wood, University of Western Hungary, Sopron, 13-15 September 2000, 2000.
- [11] Z. Hashin, Analysis of cracked laminates: A variational approach, *Mech. of Mat.* 4 (1985) 121–136.
- [12] J. A. Nairn, On the use of shear-lag methods for analysis of stress transfer in unidirectional composites, *Mech. of Materials* 26 (1997) 63–80.
- [13] J. A. Nairn, D.-A. Mendels, On the use of planar shear-lag methods for stress-transfer analysis of multilayered composites, *Mechanics of Materials* 33 (2001) 335–362.
- [14] J. A. Nairn, Generalized shear-lag analysis including imperfect interfaces, *Advanced Composite Letters* 13 (200) 263–274.
- [15] Z. Hashin, Finite thermoelastic fracture criterion with application to laminate cracking analysis, *Journal of the Mechanics and Physics of Solids* 44 (1996) 1129–1145.
- [16] L. N. McCartney, Stress transfer mechanics for multiple perfectly bonded concentric cylinder models of unidirectional composites, National Physical Lab Report DMM(A)129.
- [17] L. N. McCartney, Analytical models of stress transfer in unidirectional composites and cross-ply laminates, and their application to the prediction of matrix/transverse cracking, in: J. N. Reddy, K. L. Reifsnider (Eds.), *Local Mechanics Concepts for Composite Material Systems*, 1992, pp. 251–282.
- [18] Z. Hashin, Thermoelastic properties of fiber composites with imperfect interface, *Mech. of Materials* 8 (1990) 333–348.
- [19] J. A. Nairn, S. R. Kim, A fracture mechanics analysis of multiple cracking in coatings, *Engr. Fract. Mech.* 42 (1992) 195–208.
- [20] J. A. Nairn, Applications of finite fracture mechanics for predicting fracture events in composites, in: *Fifth Int'l Conf. on Deformation and Fracture of Composites*, 1999, pp. 1–10.
- [21] J. A. Nairn, Finite fracture mechanics of matrix microcracking in composites, in: D. R. Moore (Ed.), *The Application of Fracture Mechanics to Polymers, Adhesives and Composites*, Elsevier Science, 2004, pp. 207–212.
- [22] J. A. Nairn, Exact and variational theorems for fracture mechanics of composites with residual stresses, traction-loaded cracks, and imperfect interfaces, *Int. J. Fract.* 105 (2000) 243–271.
- [23] J. A. Nairn, A numerical study of the transverse modulus of wood as a function of grain orientation and properties, *Holzforschung* 61 (2007) 406–413.
- [24] J. M. Hedgepeth, P. V. Dyke, Local stress concentrations in imperfect filamentary composite materials, *J. Comp. Mat.* 1 (1967) 294–309.
- [25] M.-H. Han, J. A. Nairn, Hygrothermal aging of polyimide matrix composite laminates, *Composites Part A* 34 (2003) 979–986.
- [26] G. Dill-Langer, S. Lutze, S. Aicher, Microfracture in wood monitored by confocal laser scanning microscopy, *Wood Science and Technology* 36 (6) (2002) 487–499.
- [27] W. H. Press, B. P. Flannery, S. A. Teukolsky, W. T. Vetterling, *Numerical Recipes in C: The Art of Scientific Computing*, Cambridge University Press, New York, 1988.
- [28] J. A. Nairn, Concentric cylinder calculations in a java application (2009) [cited May 22, 2009].
URL <http://woodscience.oregonstate.edu/faculty/Nairn/papers/CCCJava.zip>